ON THE REENTRY DESIGN FOR THE SOHO MISSION

E. M. Alessi[(1)], G. Tommei[(2)], I. Holbrough[(3)], and J. Beck[(3)]

[(1)]*Istituto di Fisica Applicata "Nello Carrara" – Consiglio Nazionale delle Ricerche, via Madonna del Piano 10, 50019 Sesto Fiorentino (FI), Italy, Email: em.alessi@ifac.cnr.it*

[(2)]*Università di Pisa, Dipartimento di Matematica, Largo B. Pontecorvo 5, 56127 Pisa (Italy), Email: giacomo.tommei@unipi.it*

[(3)]*Belstead Research Ltd., 387 Sandyhurst Lane, Ashford TN25 4PF (UK), Email: ian.holbrough@belstead.com, james.beck@belstead.com*

ABSTRACT

Reentry trajectories to the Earth have been recently considered as a valuable end-of-life option also for Libration Point Orbits (LPO) missions. In this work, we investigate in detail the case corresponding to SOHO. On the one hand, we show how the main uncertainties associated with the problem affect the probability of reentry and the corresponding point at the interface with the atmosphere. Monte Carlo propagations are applied to different cases of uncertainties. They correspond to the orbit determination, the efficiency of the maneuver required to target the Earth, and the characteristics of the spacecraft determining the solar radiation pressure effect. On the other hand, we provide a comparison between a classical reentry from a LEO and a hypervelocity reentry from a LPO, in terms of ground casualty area and demise percentage.

Keywords: end-of-life disposal strategy; hypersonic reentry; demise; uncertainty analysis; SOHO.

1. INTRODUCTION

Motivated by the ESA/GSP study "End-of-life disposal trajectories for libration point and highly elliptical orbit missions" [5], in [1] we designed reentry trajectories to the Earth for Libration Point Orbits (LPO) missions at the end-of-life, considering as nominal cases Herschel, SOHO and Gaia. In terms of $\Delta v-$budget and operational time, the reentry to the Earth can be considered feasible, and, compared to a reentry from a Low Earth Orbit (LEO) and also from a Highly Elliptic Orbit (HEO), the main differences consist in the time of reentry and in the uncertainties associated with the solutions. In particular, as shown by the recent studies on INTEGRAL [4, 2, 8], and the actual maneuvers implemented for INTEGRAL[1] and Cluster[2] [8], a whole reentry transfer from a HEO take years to be accomplished, while the trajectories computed for LPO last less than 1 year. Moreover, the atmospheric uncertainties playing the major role in the reentry from a LEO, namely, those associated with the drag coefficient C_D and the solar activity, are secondary for a LPO, because of the higher speed of reentry (approximately 11 km/s instead of 7.7 km/s), and the lower number of excursions through the atmosphere (at most two).

Instead, the criticalities of a reentry procedure from a LPO are due to the characteristic chaoticity of this kind of orbits, and to the different aerodynamic and thermal response of hypersonic entries. In this work, we consider SOHO as a test case, and we address the role of possible uncertainties arising from the orbit determination, the maneuver efficiency, the reflectivity coefficient C_R and area-to-mass ratio A/m. By means of Monte Carlo propagations, we estimate the probability of reentry, how the longitude and latitude corresponding to the reentry location could spread over the surface of the Earth, and how the reentry angle might change. Moreover, we provide a comparison between the ground casualty area and the demise capabilities associated with a reentry from a circular LEO and a reentry from a high eccentric LPO, considering two altitudes of fragmentation and different types of fragment.

In the actual framework of a sustainable usage of the space environment, the outcome will pave the way towards an effective assessment of the risk associated to hypervelocity reentries. As the aforementioned INTEGRAL and Cluster cases show, the reentry is being considered as the most beneficial passive safeguard for the space debris problem, also for satellites orbiting beyond the LEO region. There exist only recent studies on the dynamics and the physics corresponding to hypervelocity reentries, and this is why the work presented is innovative in the field.

[1] `http://www.esa.int/Our_Activities/Operations/Integral_manoeuvres_for_the_future`

[2] `http://www.esa.int/Our_Activities/Operations/Cluster_satellite_catches_up`

Case	t_0 (JD)	x_0	y_0	z_0	$\dot{x}_0$	$\dot{y}_0$	$\dot{z}_0$
D	2459074.5639	-1312585.3903	393411.2242	241058.8008	-0.2172005	-0.3962295	-0.2012267
ND	2458364.5504	-1399608.8141	-61034.4484	36432.0763	-0.0697453	-0.3769423	-0.1988752
ND-2	2456891.5235	-841517.3240	1028050.8781	500445.0441	-0.2777571	-0.3275089	-0.0936189

Table 1. Initial and final epoch and initial conditions (after the maneuver) corresponding to the three trajectories chosen as representative. Top: direct (D); middle: non-direct (ND); bottom: non-direct heading to a high-latitude reentry (ND-2). Geocentric equatorial reference system. Units: km, s.

Case	Δv (km/s)	tof (days)	γ (deg)	λ (deg)	ϕ (deg)	e	ν (deg)	t_{atm} (s)
D	0.0751799	93.6622	-14.9	49.3	10.2	0.99	329.9	491
ND	0.0287467	226.8163	-24.5	-172.8	25.2	0.99	310.9	387
ND-2	0.0043228	281.3566	-29.8	43.4	84.6	0.99	300.0	307

Table 2. For the three nominal trajectories, initial maneuver, time of reentry, reentry angle, longitude, latitude, eccentricity and true anomaly computed at 100 km of altitude, and time spent in the atmosphere (from 2000 km to 100 km). Top: direct (D); middle: non-direct (ND); bottom: non-direct heading to a high-latitude reentry (ND-2). Geocentric equatorial reference system.

2. BACKGROUND

The Solar & Heliospheric Observatory (SOHO) mission is a joint ESA-NASA project devoted to the study of the solar environment. Launched in 1995, it is currently orbiting around the Sun on a nominal L_1 halo orbit with an out-of-plane amplitude of about 120000 km. The analysis performed here is based on the nominal solutions computed in [1] for this mission, because it is still operational (contrary to Herschel), and because the designed reentry strategy is less demanding, in principle, in terms of operations than the one designed for Gaia (see [1]).

Note that the design of the transfer is based on a small, in many cases negligible, maneuver performed at about the operational orbit to get to the Earth-ward branch of the corresponding unstable invariant manifold. The whole trajectory is computed in a full dynamical model, starting from an initial guess obtained in the Circular Restricted Three-Body Problem. The dynamics of the unstable manifold is by definition chaotic, and thus any error, either in the physical parameters or in the maneuver application, introduced at this stage may then be amplified as much as to spoil significantly the solution implemented.

In this work, the general assumption is that the orbit of the spacecraft is well determined up to the application of the maneuver, i.e., that the uncertainty in position is up to 100 m, and the one in velocity up to 0.5 mm/s [6, 7]. The uncertainty in the maneuver is set both in modulus and direction up to the 10% of the nominal value [5, 7]. Moreover, since the solar radiation pressure (SRP) is the main orbital perturbation acting on LPO, and on the corresponding hyperbolic invariant manifold exploited to reenter, the coefficient $C_R A/m$ is also characterized by an uncertainty up to the 10% of the nominal value. Following [5, 1], the nominal value of the reflectivity coefficient is $C_R = 1.9$, and of the area-to-mass ratio $A/m = 0.0196$ m^2/kg, which accounts for both the bus and the solar arrays. Instead, for the analysis on the debris footprint and the demise of the fragments (see Sec. 4), the spacecraft is assumed as an equivalent sphere with mass of 1713 kg, radius of 1.92 m, and a projected area of 11.61 m^2, that is, without the solar panels. This is reasonable because they are broken off by aerodynamic forces at about 100 km of altitude (for circular reentry this occurs at about 95 km).

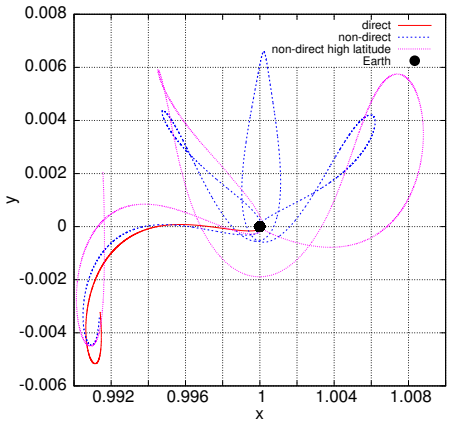

Figure 1. The three reentry trajectories taken as representative for the analysis. Sun–Earth synodical reference system with non-dimensional units.

Three illustrative orbits of reentry are considered here. The first solution is said *direct*, in the sense that the spacecraft arrives to the Earth before any other close approach; the second solution approaches the Earth–Moon neighborhood three times before reentering: the first time at an altitude of about 7900 km, and then at about 74100 km and 68200 km, respectively; the third solution first gets to an altitude of about 12000 km, then it gets away to return down to about 210000 km, and ultimately reaches the Earth at a high latitude after a journey in the L_2 region. In Figure 1 we show the three trajectories in the Sun-Earth synodical reference system, and in Table 1 the corresponding initial conditions in the geocentric equatorial reference system. In Table 2, the main features of the three reentry trajectories are listed, i.e., maneuver required Δv, time of reentry tof, reentry angle γ, longitude λ, latitude ϕ, eccentricity e and true anomaly ν (of the geocentric osculating orbit) computed at 100 km of altitude, and time spent in the atmosphere t_{atm} (from 2000 km to 100 km). The third trajectory is representative not only because it targets an area which is not populated, but also because the design of a heteroclinic connection is more prone to errors.

3. UNCERTAINTY EFFECTS

We perform a Monte Carlo analysis with an uniform distribution of the uncertainties due to the orbit determination (OD) and the maneuver, around the nominal initial conditions shown in Table 1. Every simulation consists in the propagation of 100000 initial conditions up to the nominal final epoch by means of the same differential system used to generate the nominal solutions [1]. It accounts for the gravitational attraction of the point-mass Sun, Moon, and all planets from Mercury to Pluto, SRP, atmospheric drag below 2000 km altitude, and the geopotential up to degree and order 10. The numerical integration is done by means of a Runge-Kutta-Fehlberg method of orders 7 and 8. Each propagation is done considering three values of $C_R A/m$, i.e., the nominal one, and the nominal one increased/decreased by 10%.

Whenever an altitude lower than 100 km is attained, the final state is refined in order to evaluate the dispersion in time of flight, reentry longitude, reentry latitude and reentry angle at 100 km of altitude. The final spread is estimated by computing the standard deviation with respect to the values corresponding to the nominal trajectory, but also with respect to the arithmetic mean corresponding to the population propagated. Taking as example the time of flight, we have

$$\sigma_{tof}^{nom} = \sqrt{\frac{1}{N}\sum_{i}^{N}\left(tof_i - tof_{nom}\right)^2}, \qquad (1)$$

and

$$\sigma_{tof}^{mean} = \sqrt{\frac{1}{N}\sum_{i}^{N}\left(tof_i - \bar{tof}\right)^2}, \qquad (2)$$

where N is the number of initial conditions heading to a reentry, tof_{nom} is the time of reentry for the nominal initial condition, $\bar{tof}$ the arithmetic mean of the time of reentry computed over all the reentries detected. Similar formulae apply for λ, ϕ, γ.

The results are given in Tables 3–5. We first note that the reentry is ensured for any kind of uncertainty only for the direct solution, for the non-direct one the uncertainty in the maneuver must be below the 10% of the nominal value, while for the third solution in most of the cases the reentry is lost. When the reentry is not achieved, for the non-direct transfer the spacecraft keeps wandering in the Earth neighborhood in the region delimited by L_1 and L_2. For the non-direct solution heading to a high-latitude impact point, the trajectories set forth on the external branch of the L_2 unstable manifold. In this case, we note that the solutions are extremely sensitive to the initial uncertainties. Only when the uncertainty corresponds only to the orbit determination, then the reentry is ensured, and in the neighborhood of the nominal trajectory. Under any other different assumption, the reentry turns out to be unfeasible, or achieved with a very different final configuration. Even if the maneuver is assumed to be not subject to any error, an uncertainty in the SRP effect is able to remove any possibility of reentry (the +10% case), or to move the spacecraft to a completely distant value of latitude and angle of reentry (the -10% case). This behavior is easily ascribable to the Lagrangian Point Orbits dynamics, given also the close encounters with the Earth, and the path through the L_2 neighborhood.

Focusing on the first two trajectories, the errors introduced reflect mainly on the time of flight required to get to the Earth and the corresponding σ, and thus on the longitude computed. Note the large spread computed – both σ_λ^{nom} and σ_λ^{mean} – when an uncertainty in the maneuver is assumed. In particular, comparing the first and the second trajectory, the fact that in the latter case the time of flight is more than twice than that of the former trajectory makes impossible to predict the final longitude of reentry even with only 1% of uncertainty in Δv.

Instead, when the uncertainty is associated only to the SRP, the longitude of reentry varies considerably with respect to the nominal solution, but the associated spread with respect to the other solutions computed in the Monte Carlo run is small. Similarly, it can be noticed that to add an uncertainty in SRP does not alter considerably the outcome corresponding to adding an uncertainty in Δv. In other words, the uncertainties in the final mass, shape and surface properties of the satellite are secondary, and they do not represent a critical issue. This can be explained noticing that the acceleration corresponding to the SRP is three order of magnitude lower than that due to the Earth's monopole, and the gravitational attraction exerted by Moon and Sun.

The angle of reentry is also associated with the variation in the time of flight. As shown in Figure 2 for the eccentricity at stake, there exists a well-defined correspondence between γ and the osculating true anomaly at 100 km of

uncertainty	%	$\bar{tof}$	σ_{tof}^{nom}	σ_{tof}^{mean}
OD	100	93.6622	0.0003	0.0003
OD + 10% SRP	100	93.6376	0.0246	0.0003
OD - 10% SRP	100	93.6868	0.0246	0.0003
OD + 1%Δv	100	93.5746	0.1290	0.0947
OD + 1%Δv + 10% SRP	100	93.5501	0.1467	0.0946
OD + 1%Δv - 10% SRP	100	93.5991	0.1138	0.0948
OD + 5%Δv	100	93.2339	0.6333	0.4666
OD + 5%Δv + 10% SRP	100	93.2099	0.6494	0.4661
OD + 5%Δv - 10% SRP	100	93.2580	0.6177	0.4671
OD + 10%Δv	100	92.8294	1.2386	0.9168
OD + 10%Δv + 10% SRP	100	92.8059	1.2537	0.9158
OD + 10%Δv - 10% SRP	100	92.8529	1.2237	0.9179

uncertainty	$\bar{\lambda}$	σ_{λ}^{nom}	σ_{λ}^{mean}	$\bar{\phi}$	σ_{ϕ}^{nom}	σ_{ϕ}^{mean}	$\bar{\gamma}$	σ_{γ}^{nom}	σ_{γ}^{mean}
OD	49.2	0.1	0.1	10.2	0.03	0.01	-14.9	0.03	0.01
OD + 10% SRP	58.7	9.3	0.1	10.3	0.1	0.009	-14.7	0.2	0.01
OD - 10% SRP	39.8	9.5	0.1	10.0	0.2	0.008	-15.2	0.3	0.01
OD + 1%Δv	80.8	47.7	35.8	10.0	0.6	0.6	-15.0	1.0	1.0
OD + 1%Δv + 10% SRP	90.2	54.3	35.8	10.2	0.6	0.6	-14.7	1.0	1.0
OD + 1%Δv - 10% SRP	71.5	42.2	35.9	9.9	0.7	0.6	-15.2	1.0	1.0
OD + 5%Δv	2.9	108.8	98.4	9.0	2.7	2.5	-15.8	3.9	3.8
OD + 5%Δv + 10% SRP	4.5	108.4	98.7	9.1	2.7	2.5	-15.6	3.9	3.8
OD + 5%Δv - 10% SRP	1.9	109.1	98.2	8.9	2.8	2.4	-16.0	4.0	3.8
OD + 10%Δv	-4.8	114.8	103.6	7.3	4.9	4.0	-17.8	6.9	6.2
OD + 10%Δv + 10% SRP	0.2	114.7	103.6	7.4	4.9	4.0	-17.6	6.8	6.2
OD + 10%Δv - 10% SRP	-0.3	114.9	103.6	7.2	5.0	4.0	-17.9	7.0	6.3

Table 3. Results of the Monte Carlo simulations for the direct disposal. % means percentage of reentry. Units: day, deg.

uncertainty	%	$\bar{tof}$	σ_{tof}^{nom}	σ_{tof}^{mean}
OD	100	226.8115	0.0049	0.0012
OD + 10% SRP	100	226.9056	0.0894	0.0012
OD - 10% SRP	100	226.7146	0.1016	0.0012
OD + 1%Δv	100	227.1797	0.4292	0.2282
OD + 1%Δv + 10% SRP	100	227.2628	0.4985	0.2215
OD + 1%Δv - 10% SRP	100	227.0944	0.3641	0.2350
OD + 5%Δv	100	228.0563	1.4005	0.6510
OD + 5%Δv + 10% SRP	100	228.1068	1.4345	0.6264
OD + 5%Δv - 10% SRP	100	228.0041	1.3667	0.6705
OD + 10%Δv	56.2	228.0071	1.4016	0.7392
OD + 10%Δv + 10% SRP	55.7	228.0507	1.4247	0.7112
OD + 10%Δv - 10% SRP	56.7	227.9630	1.3803	0.7681

uncertainty	$\bar{\lambda}$	σ_{λ}^{nom}	σ_{λ}^{mean}	$\bar{\phi}$	σ_{ϕ}^{nom}	σ_{ϕ}^{mean}	$\bar{\gamma}$	σ_{γ}^{nom}	σ_{γ}^{mean}
OD	-171.0	1.9	0.4	25.2	0.02	0.002	-24.4	0.05	0.02
OD + 10% SRP	154.2	33.0	0.4	25.4	0.1	0.001	-24.8	0.3	0.02
OD - 10% SRP	-135.1	37.7	0.4	25.1	0.2	0.002	-24.0	0.4	0.02
OD + 1%Δv	27.9	220.3	90.7	25.6	0.4	0.2	-24.8	0.3	0.1
OD + 1%Δv + 10% SRP	23.0	211.7	80.5	25.7	0.5	0.2	-25.0	0.5	0.1
OD + 1%Δv - 10% SRP	20.7	218.2	100.8	25.4	0.3	0.2	-24.5	0.2	0.2
OD + 5%Δv	-31.8	170.8	96.3	25.4	0.8	0.8	-20.7	6.0	4.7
OD + 5%Δv + 10% SRP	-35.5	168.1	97.0	25.4	0.9	0.8	-20.7	6.2	4.9
OD + 5%Δv - 10% SRP	-28.8	172.7	95.3	25.4	0.7	0.7	-20.7	5.8	4.5
OD + 10%Δv	-30.9	170.3	94.2	24.9	1.5	1.5	-19.7	8.0	6.5
OD + 10%Δv + 10% SRP	-34.2	167.6	94.3	25.0	1.5	1.5	-19.8	8.0	6.6
OD + 10%Δv - 10% SRP	-27.9	172.8	94.0	24.8	1.5	1.5	-19.6	8.1	6.4

Table 4. Results of the Monte Carlo simulations for the non-direct disposal. Units: day, deg.

uncertainty	%	$\bar{tof}$	σ_{tof}^{nom}	σ_{tof}^{mean}
OD	100	281.3447	0.0467	0.0454
OD + 10% SRP	0	N/A	N/A	N/A
OD - 10% SRP	100	273.0533	8.3032	0.0179
OD + 1%Δv	36.4	283.2934	2.5670	1.6850
OD + 1%Δv + 10% SRP	19.2	306.4523	25.2381	2.6781
OD + 1%Δv - 10% SRP	9.6	276.7084	5.3030	2.5524
OD + 5%Δv	14.5	281.2280	3.0488	3.0460
OD + 5%Δv + 10% SRP	24.5	279.1976	4.4087	3.8439
OD + 5%Δv - 10% SRP	3.2	278.3371	4.8628	3.8119
OD + 10%Δv	25.7	282.1731	3.2889	3.1860
OD + 10%Δv + 10% SRP	24.0	283.9801	3.3784	2.1286
OD + 10%Δv - 10% SRP	20.2	279.8072	4.0666	3.7598

uncertainty	$\bar{\lambda}$	σ_{λ}^{nom}	σ_{λ}^{mean}	$\bar{\phi}$	σ_{ϕ}^{nom}	σ_{ϕ}^{mean}	$\bar{\gamma}$	σ_{γ}^{nom}	σ_{γ}^{mean}
OD	47.0	15.2	14.7	84.7	0.1	0.05	-29.8	0.05	0.03
OD + 10% SRP	N/A	N/A	N/A	N/A	N/A	N/A	N/A	N/A	N/A
OD - 10% SRP	118.2	145.5	124.8	26.2	58.4	1.0	-0.5	29.3	0.26
OD + 1%Δv	-1.4	114.0	105.5	77.3	10.4	7.4	-28.2	2.1	1.4
OD + 1%Δv + 10% SRP	-0.7	112.5	103.5	57.6	30.7	14.7	-26.1	12.7	12.1
OD + 1%Δv - 10% SRP	2.7	112.5	104.9	66.3	23.9	15.3	-23.8	9.9	7.9
OD + 5%Δv	0.8	113.1	104.8	73.7	15.3	10.8	-31.3	7.2	7.0
OD + 5%Δv + 10% SRP	-2.6	113.3	103.6	55.9	29.5	6.8	-40.8	15.6	11.0
OD + 5%Δv - 10% SRP	2.1	112.9	105.1	68.3	21.7	14.3	-24.7	8.8	7.1
OD + 10%Δv	-0.5	112.7	103.8	59.0	29.6	14.8	-22.3	12.0	9.3
OD + 10%Δv + 10% SRP	1.4	108.9	101.5	57.0	30.3	12.6	-22.8	12.1	9.9
OD + 10%Δv - 10% SRP	-0.1	112.6	103.9	58.9	31.0	17.2	-21.8	13.5	10.8

Table 5. Results of the Monte Carlo simulations for the non-direct disposal heading to a high-latitude reentry. Units: day, deg. The larger σ_{tof}^{nom} for the case OD+1%Δv + 10% SRP is due to the fact that we allowed a longer window to reenter.

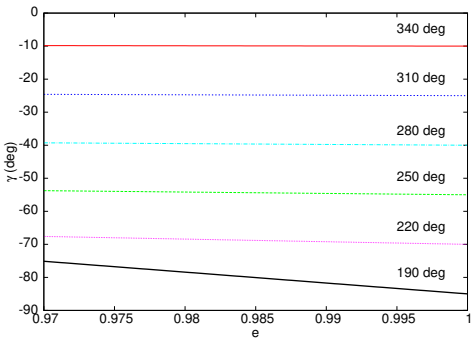

Figure 2. Angle of reentry γ as a function of the geocentric eccentricity e and true anomaly (the label at the lines) computed at 100 km of altitude, for the eccentricity values of interest.

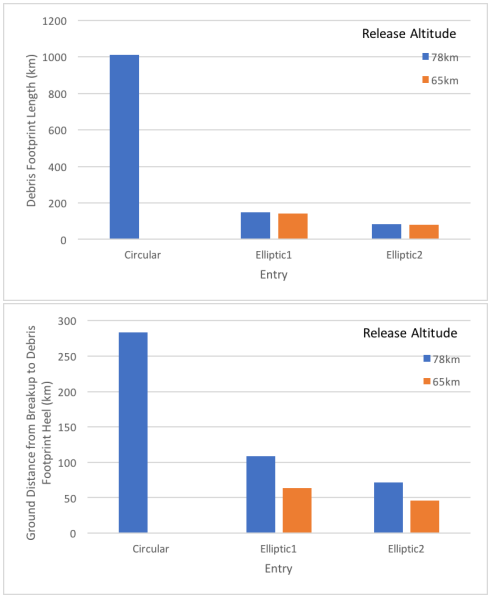

Figure 3. Debris footprint length (top) and ground distance from the fragmentation point to the debris footprint heel as a function of the type of entry and fragmentation altitude.

altitude, which is, in turn, the time spent on the given parabolic orbit.

4. DEBRIS FOOTPRINT AND DEMISE

In order to get an insight on the consequences of a fragmentation corresponding to a reentry from a LPO, the final leg of the trajectory, that is, from about 110 km of altitude down to the ground, is simulated using the BRL's 3DOF code ATS3 with SAM heating correlations [3, 9]. We show here the results corresponding to the direct and non-direct reentry, compared with a hypothetical reentry of SOHO from a circular sun-synchronous orbit. The analysis is focused on two nominal altitudes of breakup, namely, 78 km and 65 km. The latter value is set considering a balance between the dynamic pressure and the heat soak experienced during the hypervelocity reentry. That is, the deceleration the spacecraft is subject is much higher than the standard case, but the heat soak is not because of the shorter time spent in the atmosphere.

DIRECT/CIRCULAR					
	Ballistic Coefficient (kg/m^2)				
Mass (kg)	**4**	**20**	**50**	**200**	**700**
0.5	both	both	both	both	N/A
1.0	both	both	both	both	N/A
5.0	both	both	both	both	circular
10	both	both	both	circular	9.4
50	N/A	0.7	2.1	3.8	3.4

NON-DIRECT/CIRCULAR					
	Ballistic Coefficient (kg/m^2)				
Mass (kg)	**4**	**20**	**50**	**200**	**700**
0.5	both	both	both	both	N/A
1.0	both	both	both	both	N/A
5.0	both	both	both	circular	circular
10	both	both	circular	circular	23.1
50	N/A	2.3	5.8	7.6	5.3

Table 6. Ratio of mass landed from the direct (top) or non-direct (bottom) LPO reentry and the mass landed from the circular orbit. The altitude of fragmentation is assumed at 78 km, and the fragments made of aluminum. 'Both' means that both reentries demise completely; 'circular' only the circular one.

At the breakup, a catalogue of solid, spherical fragments of different radii, material (aluminum or steel), and hypersonic ballistic coefficients are released ($C_D = 0.915$). The state of the parent SOHO vehicle, inclusive of its temperature, is transferred to each of the fragments and the resulting trajectories are propagated to either impact with the ground or the point at which they are predicted to have a terminal energy below the 15J necessary to inflict injury.

In Figure 3, we give the along-track length of the debris field, and the ground distance from the point of breakup to the heel of the debris field. A steeper reentry has a beneficial impact on the size of the footprint, and the altitude of fragmentations plays a minor role.

Concerning the demise, the conclusions are more sensitive to the assumptions made. In Tables 6-9 we show the results as the ratio between the mass landed in case of an elliptic reentry from the LPO and the mass landed in case of a circular reentry. For aluminum, in most circumstances both entry types have similar performance, with fully demising the fragment. However, for fragments of

DIRECT/CIRCULAR					
	Ballistic Coefficient (kg/m^2)				
Mass (kg)	**4**	**20**	**50**	**200**	**700**
0.5	both	both	both	both	N/A
1.0	both	both	both	both	N/A
5.0	both	both	both	circular	circular
10	both	both	circular	circular	10.6
50	N/A	2.9	4.5	4.7	3.4

NON-DIRECT/CIRCULAR					
	Ballistic Coefficient (kg/m^2)				
Mass (kg)	**4**	**20**	**50**	**200**	**700**
0.5	both	both	both	both	N/A
1.0	both	both	both	both	N/A
5.0	both	both	both	circular	circular
10	both	circular	circular	circular	24.4
50	N/A	5.1	8.8	8.5	5.3

Table 7. Ratio of mass landed from the direct (top) or non-direct (bottom) LPO reentry and the mass landed from the circular orbit. The altitude of fragmentation is assumed at 65 km, and the fragments made of aluminum. 'Both' means that both reentries demise completely; 'circular' only the circular one.

DIRECT/CIRCULAR					
	Ballistic Coefficient (kg/m^2)				
Mass (kg)	**4**	**20**	**50**	**200**	**700**
0.5	elliptic	elliptic	elliptic	both	N/A
1.0	elliptic	elliptic	elliptic	both	N/A
5.0	0.9	elliptic	elliptic	elliptic	1.1
10	1.0	0.1	elliptic	0.2	1.1
50	N/A	0.9	0.7	0.9	1.0

NON-DIRECT/CIRCULAR					
	Ballistic Coefficient (kg/m^2)				
Mass (kg)	**4**	**20**	**50**	**200**	**700**
0.5	elliptic	elliptic	elliptic	both	N/A
1.0	elliptic	elliptic	elliptic	both	N/A
5.0	0.6	both	both	0.5	3.7
10	1.0	0.2	0.2	0.6	2.3
50	N/A	1.0	1.0	1.0	1.0

Table 8. Ratio of mass landed from the direct (top) or non-direct (bottom) LPO reentry and the mass landed from the circular orbit. The altitude of fragmentation is assumed at 78 km, and the fragments made of steel. 'Both' means that both reentries demise completely; 'elliptic' only the elliptic one.

high mass and high ballistic coefficient, the elliptic reentry is clearly more detrimental. Lowering the altitude of fragmentation or considering a steeper reentry angle, the situation gets worse. As shown in Figure 4, the slower circular entry results in greater heating of the parent body leading to a higher initial temperature, and the fragment reaching its melting point at a higher altitude. This, combined with a slower initial decent through the atmosphere leads to fragments returning from a circular orbit experiencing greater heating, and therefore, demise. This mechanics holds because the aluminum has a low melting point.

If the fragments are instead made of steel, an elliptic reentry turns out to be advantageous. Despite the significantly higher initial temperature of the fragment entering from a circular orbit, the heating profile (see Figure 5) results in a longer but relatively lower intensity one than in the case of an elliptic reentry. In other words, reentering from a circular orbit, the heat fluxes are insufficiently high for the radiative equilibrium temperature to be above the melt temperature for steel, and thus demise cannot occur. On the other hand, it can be seen that very steep high velocity entries can also result in fragments failing to reach the material melting point. In this case although the fluxes are higher, the heating period is too short to deliver the heat load required to the raise the temperature of the fragment to melting point. The same is true when the altitude of fragmentation is lower. Looking the corresponding tables, it is clear that mass and ballistic coefficient play both a major role for the mechanism.

Finally, the simulations reveal the relative insensitivity of casualty risk to the demise and the consequent importance of fully demising fragments.

5. CONCLUSIONS

In this work, we have analyzed hypersonic highly elliptic reentries from a Libration Point Orbit, in terms of orbit uncertainties and risk on the ground. The uncertainty in the maneuver required to target the Earth, even if small, can alter dramatically the reentry conditions, in particular the probability of success and the longitude of arrival. The latter issue is the same faced by circular reentries, although in that case the impossibility of predicting the final point is due to the atmospheric uncertainties. For an elliptic transfer, however, in case of a confirmed risk, the high speed makes the time available to alert too short. To overcome the high spread in the longitude of impact, a correction maneuver is foreseen. This would also ensure to reenter, when the transfer designed is a non-direct one. The crucial problem to be solved in the future is the time when this maneuver shall be applied. The spacecraft should be sufficiently close to the Earth to avoid an excessive amplification of the errors, but sufficiently far to permit a precise orbit determination, and take all the preventative measures.

Concerning the last leg of the reentry, the conditions ex-

DIRECT/CIRCULAR					
	Ballistic Coefficient (kg/m^2)				
Mass (kg)	**4**	**20**	**50**	**200**	**700**
0.5	elliptic	elliptic	elliptic	both	N/A
1.0	elliptic	elliptic	elliptic	both	N/A
5.0	1.0	0.1	elliptic	0.2	1.6
10	1.0	0.4	0.2	0.3	1.4
50	N/A	1.0	1.0	1.0	1.0

NON-DIRECT/CIRCULAR					
	Ballistic Coefficient (kg/m^2)				
Mass (kg)	**4**	**20**	**50**	**200**	**700**
0.5	elliptic	elliptic	elliptic	both	N/A
1.0	elliptic	elliptic	elliptic	both	N/A
5.0	1.0	0.2	0.1	0.7	4.4
10	1.0	0.5	0.4	0.8	2.3
50	N/A	1.0	1.0	1.0	1.0

Table 9. Ratio of mass landed from the direct (top) or non-direct (bottom) LPO reentry and the mass landed from the circular orbit. The altitude of fragmentation is assumed at 65 km, and the fragments made of steel. 'Both' means that both reentries demise completely; 'elliptic' only the elliptic one.

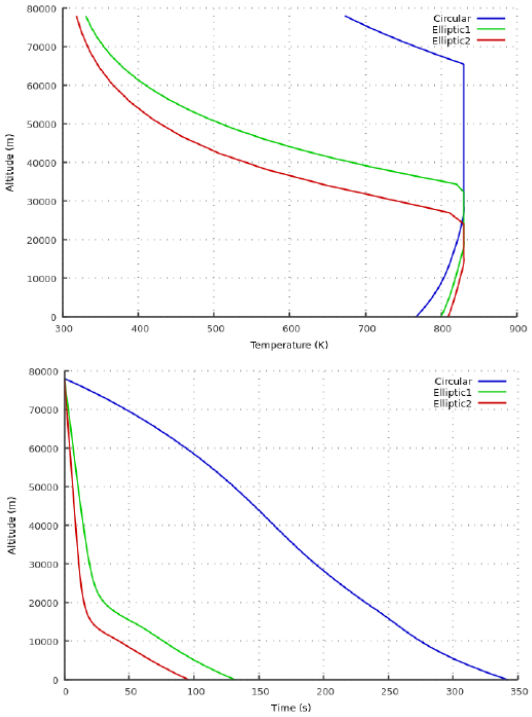

Figure 4. Temperature/altitude profile (top) and altitude as a function of time (bottom) for 50 kg and 700 kg/m^2 aluminum fragment released at 78 km.

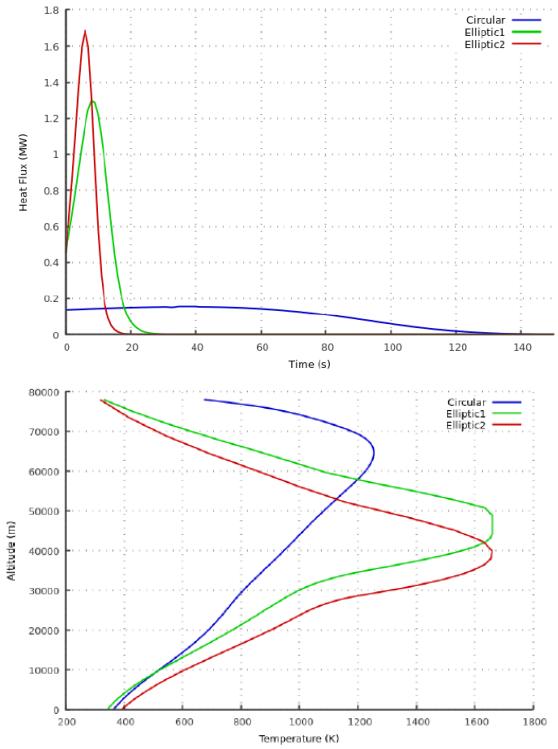

Figure 5. Heat flux as a function of time (top) and temperature/altitude profile (bottom) for 50 kg and 700 kg/m^2 steel fragment released at 78 km.

perienced by and debris field resulting from steep elliptic entries differ significantly from those associated with circular entries. The steep entry and the shorter period in the atmosphere cause the debris field to be significantly shorter in length and closer to the point of breakup than those associated with circular entries. Although the altitude at which fragmentation is assumed to occur does have some influence on the dimensions and location of the debris field, it is relatively minor. The demise of fragments is a complex balance between the heat fluxes delivered to the fragment, the duration of heating and the fragment material. As such, it is not possible to optimize the demise of all fragments within a catalogue, or to provide globally applicable recommendations to improve fragment demise, but this is true also for a standard reentry from a circular orbit. In the entries considered it can be seen that the elliptic entries result in marginally less demise than a circular entry for less resistant aluminium. However, the opposite is found for steel fragments where demise is constrained by the lower fluxes of the circular entry failing to raise the fragment temperature to the melting point of steel.

ACKNOWLEDGMENTS

We are grateful to Bernhard Fleck and Daniel Mattern for providing the covariance matrix corresponding to recent orbit determination performed for SOHO, and for the discussion on the uncertainty to be applied to the maneuver.

Part of this work is funded through the European Commission Horizon 2020, Framework Programme for Research and Innovation (2014-2020), under the ReDSHIFT project (grant agreement n° 687500).

REFERENCES

1. Alessi, E. M., (2015). The reentry to Earth as a valuable option at the end-of-life of Libration Point Orbit missions. *Adv. Space Res.*, **55**(12), 2914–2930
2. Armellin, R., San-Juan, J. F., Lara, M., (2015). End-of-Life Disposal of High Elliptical Orbit Missions: the case of INTEGRAL. *Adv. Space Res.*, **56**(3), 479–493
3. Beck, J., Merrifield, J., Holbrough, I., Markelov, G., Molina, R., (2015). Application of the SAM Destructive Re-entry Code to the Spacecraft Demise Integration Test Cases. 8th European Symposium on Aerothermodynamics for Space Vehicles, Lisbon, Portugal
4. Colombo, C., Letizia, F., Alessi, E. M., Landgraf, M., (2014a). End-of-life Earth re-entry for highly elliptical orbits: the INTEGRAL mission. AAS/AIAA Space Flight Mechanics Meeting, Santa Fe, New Mexico, U.S.A., AAS paper 14-156
5. Colombo, C., Letizia, F., Soldini, S., Lewis, H., Alessi, E. M., Rossi, A., Vasile, M., Vetrisano, M., Van der Weg, W., (2014b). End-of-life disposal trajectories for libration point and highly elliptical orbit missions, Final Report, ESA/ESOC contract No. 4000107624/13/F/MOS
6. Fleck, B., (2015). SOHO Project Scientist & Mission Manager, ESA at NASA GSFC. Private Communication
7. Mattern, D. W., (2015). NASA GSFC, Omitron, Inc., Flight Dynamics Facility. Private Communication
8. Merz, K., Krag, H., Lemmens, S., Funke, Q., Böttger, S., Sieg, D., Ziegler, G., Vasconcelos, A., Sousa, B., Volpp, H.-J., Southworth, R., (2015). Orbit Aspects of End-Of-Life Disposal from Highly Eccentric Orbits. 25th International Symposium on Space Flight Dynamics, Munich, Germany
9. Merrifield J., Beck J., Markelov G., Leyland P., Molina R. (2015) Aerothermal Heating Methodology in the Spacecraft Aerothermal Model (SAM). In: Sgobba T., Rongier I. (eds) Space Safety is No Accident. Springer, Cham